machines

MDPI

Article

NiTi Alloy Quasi-Zero Stiffness Vibration Isolation Structure with Adjustable Mechanical Properties

Qian Wu [1], Jianxiang Qiao [2], Xinping Li [1], Shengsheng Wang [1,2], Bingqian Li [3], Siyang Wu [4], Zhenguo Wang [3,*] and Jiangtao Ji [1]

[1] College of Agricultural Equipment Engineering, Henan University of Science and Technology, Luoyang 471003, China; zwuqian@haust.edu.cn (Q.W.); aaalxp@126.com (X.L.); ws@haust.edu.cn (S.W.); jjt0907@163.com (J.J.)
[2] State Key Laboratory of Intelligent Agricultural Power Equipment, Luoyang 471039, China; qiaojx0719@foxmail.com
[3] Key Laboratory of Bionic Engineering (Ministry of Education), Jilin University, Changchun 130022, China; bqli@jlu.edu.cn
[4] College of Engineering and Technology, Jilin Agricultural University, Changchun 130118, China; wsy@jlau.edu.cn
* Correspondence: zgwang24@jlu.edu.cn

Abstract: Despite the significant engineering applications of vibration isolation structures, there remain challenges in adjusting low-frequency isolation performance. To tackle this issue, this study proposes a temperature-controlled quasi-zero stiffness vibration isolation structure utilizing NiTi shape memory alloys. The stiffness and vibration isolation performance of the structure can be adjusted by modifying the heat treatment process and temperature variations of the alloy. The vibration isolation system is composed of vertical and horizontal alloy beams, with structural mechanics analysis performed to develop both static and dynamic theoretical models. The study investigates the effects of the heat treatment process on the phase transition characteristics and mechanical properties of nickel-titanium alloys, and analyzes the correlation between the heat treatment parameters of alloy beams and the stiffness performance of vibration isolation structures. By applying temperature variations to the alloy beams, the stiffness and vibration isolation performance of the entire structure can be dynamically adjusted. This research provides theoretical guidance for achieving adjustable vibration isolation performance across low-frequency and wide ranges, offering promising prospects for the application of vibration isolation structures in dynamic environments.

Keywords: quasi-zero stiffness; vibration isolation structure; NiTi shape memory alloys; low frequency

Academic Editor: Swee Leong Sing

Received: 11 December 2024
Revised: 20 January 2025
Accepted: 21 January 2025
Published: 24 January 2025

Citation: Wu, Q.; Qiao, J.; Li, X.; Wang, S.; Li, B.; Wu, S.; Wang, Z.; Ji, J. NiTi Alloy Quasi-Zero Stiffness Vibration Isolation Structure with Adjustable Mechanical Properties. *Machines* **2025**, *13*, 92. https://doi.org/10.3390/machines13020092

1. Introduction

Vibration is prevalent in engineering systems, whether originating from the operation of the equipment itself or induced by the surrounding environment. Such vibrations can adversely affect precision instruments, mechanical equipment, aerospace devices, and vehicle systems [1–4]. In vibration control, isolators are commonly used to achieve effective vibration isolation [5–7]. Conventional linear vibration isolators typically consist of linear springs, damping elements, and a load mass [8,9]. They are effective at attenuating vibrations only when the excitation frequency is significantly higher than the system's natural frequency ($\sqrt{k/m}$) [10]. The natural frequency is influenced by the system's stiffness k and mass m, so achieving low-frequency isolation generally requires reducing the load-bearing capacity of the isolator [11–13]. However, linear vibration isolators cannot simultaneously achieve both high load-bearing capacity and low-frequency isolation, limiting their practical engineering applications. Additionally, these isolators have a fixed isolation frequency range, making them less adaptable to complex operational environments.

Recently, researchers have focused on the development of nonlinear vibration isolators with high static and low dynamic stiffness that can support large static loads while isolating low-frequency vibrations [14–16]. Quasi-zero-stiffness (QZS) structures, characterized by high-static and low-dynamic stiffness, are considered effective for low-frequency vibration isolation [17–21]. Currently, QZS isolators require a combination of positive and negative stiffness, functioning effectively only within a narrow load range [22–24]. The fixed configuration of QZS vibration isolation structures limits the tunability of their mechanical properties, thereby constraining their application potential. Consequently, there is a pressing need to develop isolation structures with a broader frequency range and adjustable isolation capabilities to enhance their practical applicability.

Shape memory alloys (SMAs) are intelligent metallic materials capable of "remembering" their original shapes [25–28]. SMAs exhibit two distinct macroscopic mechanical properties: shape memory effect (SME) and superelasticity (SE), both of which are induced by phase transitions between austenite and martensite within the material [29,30]. These transitions lead to dual changes in structure and properties under the influence of external forces and/or temperature [31]. Additionally, shape memory alloys (SMAs) exhibit advantageous properties, including hysteresis behavior and high damping capacity, making them well-suited for high-performance vibration isolation structures [32,33]. NiTi shape memory alloy stands out due to its excellent memory characteristics, high strength, and adjustable properties, making it the preferred material for high-performance tunable devices. Thus, the significant modulus variation in the alloy enhances the potential for vibration isolation structures to achieve a wide range of tunable isolation performance.

In this study, vibration isolation structures with customizable and tunable stiffness and isolation performance were fabricated using NiTi shape memory alloy. The structure consists of vertical and horizontal beams, and a structural mechanics analysis was conducted to establish both static and dynamic theoretical models. The effects of heat treatment processes (time and temperature) on the phase transition characteristics of the NiTi alloy beams and the vibration isolation performance of the structure were studied, systematically analyzing the effects of heat treatment on phase transition temperatures and mechanical properties. By programming the temperature of the alloy vibration isolation structure, the mechanical properties were controlled to allow tunability of stiffness, load capacity, and vibration isolation performance. Furthermore, by controlling the temperature of the alloy beams, the stiffness and isolation performance of the vibration isolation structure was further adjusted.

2. Design and Materials

2.1. The Configuration Designs and Theoretical Analysis of Vibration Isolation Structures

The NiTi alloy element used in this study is initially heat-treated to a straight shape. Upon installation into the vibration isolation structure, the SMA element undergoes deformation due to the applied pre-load and operational forces, resulting in the curved shape shown in Figure 1. Figure 1a illustrates the NiTi vibration isolation structure, which comprises a single horizontal and two vertical cosine beams connected via a frame and crossbeam. The horizontal cosine beam traverses the crossbeam and is linked to the vertical cosine beam and the frame. The vertical cosine beam is connected to the crossbeam and the frame. The crossbeam is guided by the rails, which enable it to slide vertically. When subjected to vertical loads, the horizontal cosine beam displays negative stiffness, while the vertical cosine beam exhibits positive stiffness. So, the two can be integrated in certain ways to achieve zero stiffness. As shown in Figure 1b, the geometrical model of the horizontal cosine beam is defined as follows:

$$y = \frac{h_1}{2\left[1 - cos\left(\frac{2\pi x}{l_1}\right)\right]} \tag{1}$$

where h_1 is the initial height of the beam vertex, t_1 is the thickness of the beam, b_1 is the width, and l_1 is the span.

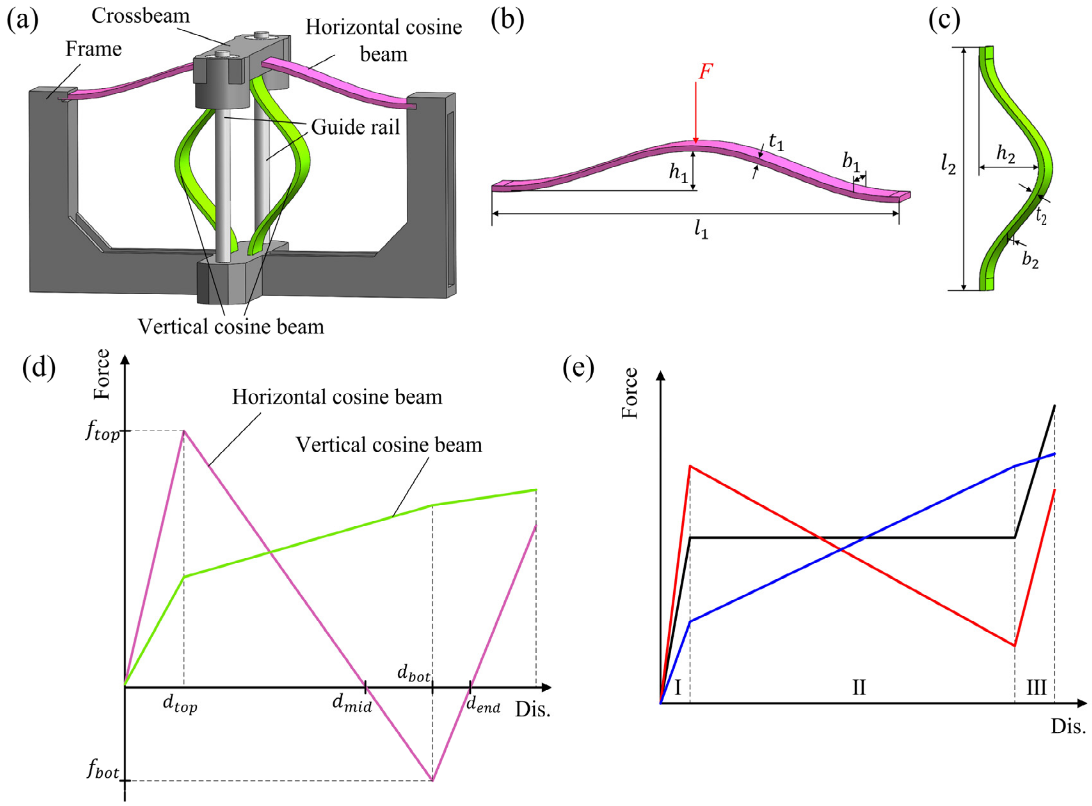

Figure 1. The vibration isolation structure diagram and its theoretical analysis: (**a**) The schematic diagram of the vibration isolation structure. (**b**) The parameters of the horizontal cosine beam. (**c**) The parameters of the vertical cosine beam. (**d**) The force–displacement curve of the horizontal cosine beam and the vertical cosine beam. (**e**) The force–displacement curve of the vibration isolator.

As shown in Figure 1c, the geometrical model of the vertical cosine beam is defined as follows:

$$x = \frac{h_2}{2\left[1 - cos\left(\frac{2\pi y}{l_2}\right)\right]} \tag{2}$$

where h_2 is the initial height of the beam vertex, t_2 is the thickness, b_2 is the width, and l_2 is the span.

Combining horizontal and vertical cosine beams with different parameters creates various stiffness properties, including positive, zero, and negative stiffness.

According to Jin [34] et al., when the cosine end is constrained by the fixed constraint, the external load F is applied at the middle vertex of the beam, which can be expressed as:

$$F = \frac{3\pi^2 Q^2}{2}\Delta\left(\Delta - \frac{3}{2} + \sqrt{\frac{1}{4} - \frac{4}{3Q^2}}\right)\left(\Delta - \frac{3}{2} - \sqrt{\frac{1}{4} - \frac{4}{3Q^2}}\right) \tag{3}$$

where $Q = \frac{h}{t}$, $\Delta = d/h$.

Therefore, when the dimensionless parameter Q of the cosine beam $Q = h_1/t_1 \geq 6$, the force–displacement curve can be represented by three connected lines [35–37], as shown in Figure 1d,e, and the variation in stiffness is as follows:

$$f_{top} \approx 8\pi^4 \frac{E_1 I_1 h_1}{l_1^3},\ f_{bot} \approx -4\pi^4 \frac{E_1 I_1 h_1}{l_1^3},\ d_{min} = \frac{4}{3} h_1 \tag{4}$$

$$d_{top} \approx \frac{8t_1^2}{3h_1},\ d_{bot} \approx 2h_1 - \frac{8t_1^2}{3h_1},\ d_{end} \approx 2h_1 - \frac{4t_1^2}{3h_1} \tag{5}$$

Assuming that the horizontal cosine beam is loaded uniformly, the stiffness equations for the three stages of the horizontal cosine beam are as follows (E_2, Young's modulus, I_2, the moment of inertia):

$$k_{l1} \approx \frac{8\pi^4 E_1 I_1 h_1^2}{l_1^3 t_1^2},\ k_{l2} \approx \frac{18\pi^4 E_1 I_1 h_1^2}{l_1^3 \left(3h_1^2 - 8t_1^2\right)},\ k_{l3} \approx \frac{3\pi^4 E_1 I_1 h_1^2}{l_1^3 t_1^2} \tag{6}$$

The vertical cosine beam primarily provides positive stiffness within the overall structure. The force–displacement curve under vertical load is illustrated in Figure 1d. The vertical cosine beam exhibits nonlinear stiffness, which can be divided into three segments, each of which resembles a linear relationship. Consequently, each segment has a constant stiffness. The stiffness of the three segments of the force–displacement curve for the vertical cosine beam is as follows:

$$k_v = \begin{cases} a\frac{E_2 I_2 h_2^2}{l_2^3 t_2^2},\ 0 < d < d_{top} \\ b\frac{E_2 I_2 h_2^2}{l_2^3 t_2^2},\ d_{top} \leq d \leq d_{bot} \\ c\frac{E_2 I_2 h_2^2}{l_2^3 t_2^2},\ d_{bot} < d < d_{end} \end{cases} \tag{7}$$

where a, b, and c are three dimensionless parameters. The dimensionless parameters for different elastic moduli and moments of inertia can be obtained through elastic analysis.

Under vertical load, the horizontal and vertical cosine beams have the same direction of stiffness, so the overall vertical stiffness of the structure is the sum of the stiffnesses of the segments. The force–displacement curve can be divided into the following three stages:

$$k_1 = k_{l1} + 2k_v,\ k_2 = k_{l2} + 2k_v,\ k_2 = k_{l2} + 2k_v \tag{8}$$

As illustrated in Figure 1e, by matching the structural parameters of the horizontal and vertical cosine beams, it is possible to tailor the stiffness of distinct regions across the overall structural force–displacement curves, thereby enabling the customization of the overall structural stiffness (positive, zero, and negative). In the vibration isolation structure, the structural parameters of the programmed cosine beams are optimized to achieve high-static stiffness and dynamic-zero stiffness, which enables the structure to carry static loads and isolate vibrations, respectively.

Therefore, as shown in Table 1, the geometric parameters of the vibration isolation structure are selected to study the vibration isolation performance at different temperatures.

Table 1. The geometric parameters of the vibration isolation structure.

t_1 (mm)	b_1 (mm)	h_1 (mm)	l_1 (mm)	t_2 (mm)	b_2 (mm)	h_2 (mm)	l_2 (mm)
0.2	10	12	70	0.2	10	5	40

2.2. Material Preparation and Characterization

In this study, the NiTi memory alloy sheet (temperature-controlled shape memory alloy, Suzhou Oceanpower Rare Metals Co., Ltd., Suzhou, China) is employed to conduct experimental research. The thickness of the plate is 0.2 mm, and its composition is shown in Table 2.

Table 2. The composition and content of NiTi alloy.

Component Content										
Ni (wt.%)	**C (wt.%)**	**Co (wt.%)**	**Cu (wt.%)**	**Cr (wt.%)**	**Nb (wt.%)**	**Fe (wt.%)**	**O (m/m)**	**N (m/m)**	**H (m/m)**	**Ti**
55.8	0.0074	<0.003	<0.003	<0.003	<0.003	0.004	0.034	0.0015	0.007	Remain

The phase transformation temperature of the NiTi alloy is controlled through heat treatment to obtain different shape memory properties and superelasticity, which supports further programming and customization of vibration isolation structures [38–40]. So, the NiTi alloy is heat-treated using a box-type atmosphere furnace (MXQ1400-20, Shanghai Weixing Furnace Industry Co., Ltd., Shanghai, China) to investigate the effects of heat treatment on its thermodynamic properties. In the heat treatment process, the NiTi alloy sheet is cut into rectangular specimens (70 mm × 5 mm × 0.2 mm) by wire-cutting technology. The furnace is then heated to the specified temperature and held for 30 min before the specimens are heat treated at 450–510 °C for 5–20 min. Finally, the alloy is rapidly quenched in water at 20 °C. The detailed process parameters are shown in Table 3.

Table 3. The heat treatment process for the TiNi alloy.

Temperature (°C)	**450**	**470**	**490**	**510**
Time (min)	5 10 15 20	5 10 15 20	5 10 15 20	5 10 15 20

The NiTi alloy has two crystalline structures, namely, martensite and austenite, which exhibit endothermic or exothermic phenomena during phase transitions. Therefore, differential scanning calorimetry (DSC25, TA Instruments) is employed to study the phase transformation characteristics. Alloy wires are cut into samples 1.5 mm to 2.0 mm in length and placed in the analyzer's crucible, undergoing cooling and heating at 10 °C/min between −50 °C and 150 °C. The phase transition temperature of the NiTi alloy varies with different heat treatment processes, leading to different DSC data. By analyzing the characteristics of the DSC curves, we can gain insights into the alloy's phase transition behavior and transition temperatures.

A microcomputer-controlled universal testing machine (WH-5500, Ningbo Weiheng Testing Instrument Co., Ltd., Ningbo, China) is used to investigate the mechanical properties of NiTi alloys and vibration isolation structures. The quasi-static tensile tests were performed at a strain rate of 0.5 mm/min, which is consistent with standard testing procedures for shape memory alloys as defined by ASTM E8/E8M. This strain rate was chosen to ensure accurate measurement of the alloy's elastic and plastic deformation behaviors under controlled conditions. This testing approach allows us to measure the alloy's elastic modulus, yield strength, and strain at different temperatures. Additionally, quasi-static compression tests are performed at a strain rate of 30 mm/min to examine the static mechanical properties of various NiTi alloy vibration isolation structures.

A DC power supply (Mastech DP6020, Shenzhen Ouruijia Technology Co., Ltd., Shenzhen, China) is used to heat the NiTi alloy vibration isolation structure under a constant current of 6 A to investigate the influence of voltage on temperature. We use a temperature sensor (WZPK-100, Hangzhou Meaco Sensor Technology Co., Ltd., Hangzhou, China) and an infrared thermal imager (FLIR E40, Shenzhen Yida Intelligent Technology Co., Ltd., Shenzhen, China) to measure the temperatures of the vibration isolation structure at different voltages.

3. Results and Discussions

3.1. The Heat Treatment for the Phase Transformation Behavior of SMA

During the DSC test, martensitic or reverse martensitic phase transformations occur within the material, leading to changes in the crystal structure, which correspond to exothermic or endothermic peaks on the DSC curve.

In this study, the double-tangent method is used to determine the martensitic start temperature (M_s), martensitic end temperature (M_f), austenitic start temperature (A_s), and austenitic end temperature (A_f), from the cooling and heating DSC curves, respectively. These temperatures are used to characterize the phase transformation temperatures of the alloy. Figure 2 and Table 4 demonstrate the influence of varying holding times on the M_s, M_f, A_s, and A_f of the NiTi alloy at a consistent heat treatment temperature. The experimental results indicate that as the holding time is extended, the M_s, M_f, A_s, and A_f temperatures of the NiTi shape memory alloy decrease.

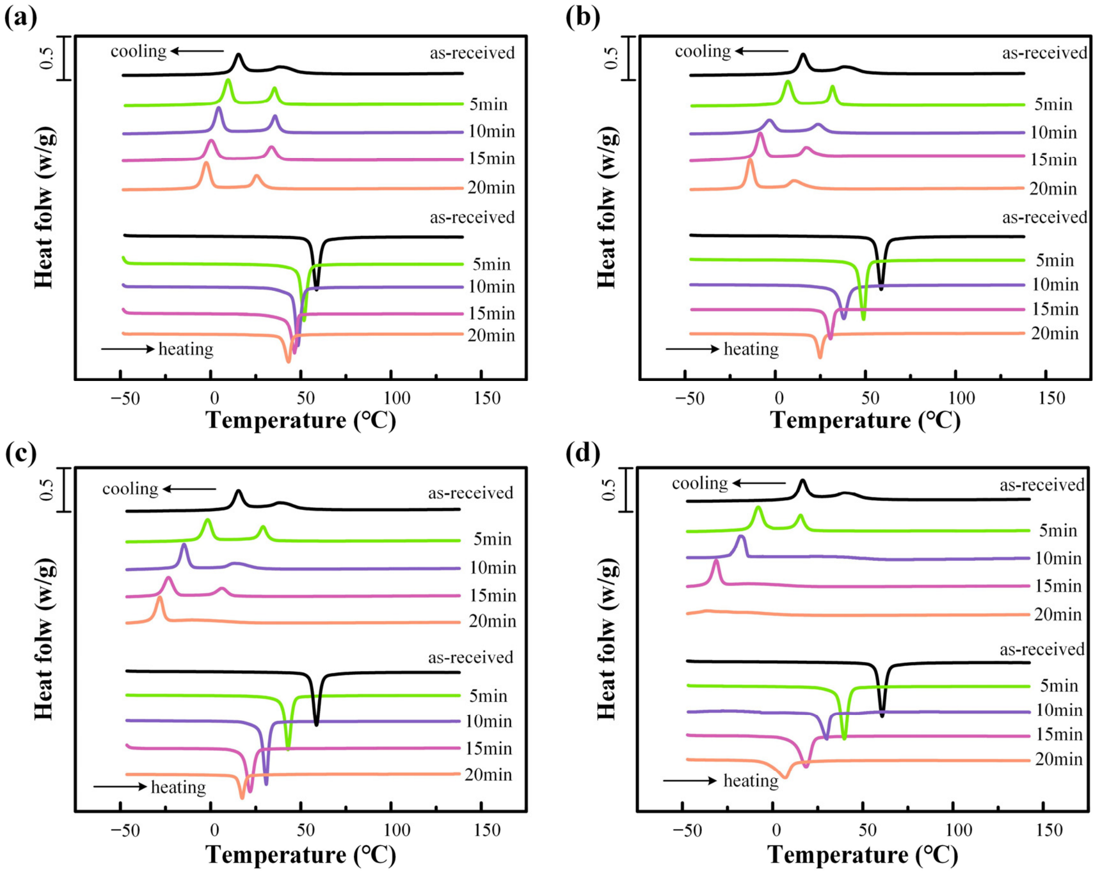

Figure 2. The DSC test results of NiTi Alloy: (**a**) 450 °C. (**b**) 470 °C. (**c**) 490 °C. (**d**) 510 °C.

As shown in Figure 2a,b, at temperatures of 450 °C and 470 °C, the DSC cooling curves for NiTi alloys exhibit two transformation peaks, namely, the R-phase and martensitic (M) transformation, corresponding to the two-step martensitic transformation (A→R→M).

The heating curve exhibits a single peak, which corresponds to the reverse martensitic transformation M→A. As shown in Figure 2c,d, at temperatures of 490 °C and 510 °C, the two peaks on the cooling curve merge with increasing holding time, reflecting an A→R→M/A→M process. This transition occurs as heat treatment time increases, the R phase in the alloy turns into the M phase, making the phase transition more stable. Consequently, the phase transformation type undergoes a gradual transition from A→R→M to A→M as the duration of the heat treatment increases.

Table 4. The effect of heat treatment on the phase transformation temperatures of the NiTi alloy.

	M_f (°C)	M_s (°C)	A_s (°C)	A_f (°C)
None	12.04	18.93	55.12	64.34
450 °C/5 min	6.5	12.86	47.64	54.86
450 °C/10 min	1.05	8.27	43.7	50.92
450 °C/15 min	−3.54	4.66	41.73	47.93
450 °C/20 min	−4.86	0.98	39.76	45
470 °C/5 min	3.44	11.09	44.52	52.4
470 °C/10 min	−7.55	1.41	33	42.6
470 °C/15 min	−12	−4.23	26.51	33.66
470 °C/20 min	−17.29	−10.24	21.62	27.53
490 °C/5 min	−6.4	2.26	39.76	46.46
490 °C/10 min	−18.57	−10.86	27.17	33.37
490 °C/15 min	−28.71	−18.24	17.72	25.75
490 °C/20 min	−32.32	−25	14.63	20.28
510 °C/5 min	−13.15	−2.72	35.24	43.04
510 °C/10 min	−23.36	−13.65	23.72	32
510 °C/15 min	−35.66	−27.62	10.47	23.46
510 °C/20 min	–	–	−3.94	11.65

The transition from the R-phase to the M-phase is a thermodynamic process that is influenced by both the temperature and the holding time during heat treatment. As the heat treatment time increases, the alloy undergoes a gradual transition from the R-phase to the more stable M-phase, which is characterized by a higher energy barrier [41,42]. This phase transformation is driven by the release of internal stresses and the rearrangement of atomic structures, leading to a more stable phase transition [43,44].

Following processing, NiTi alloys exhibit minor internal defects, including stress and dislocations. Heat treatment facilitates the release of internal stress and reduction in these defects, thereby minimizing obstacles to phase transformation. Furthermore, the reduction in defect density encourages the formation of a more uniform crystal structure, facilitating both martensitic and reverse martensitic transformations. Consequently, as the heat treatment time is increased, the phase transformation temperature will gradually decrease.

As shown in Figure 3, the heat treatment temperature significantly affects the phase transformation type of NiTi alloys. At treatment temperatures of 450 °C, 470 °C, and 490 °C, the DSC cooling curves exhibit two-phase transition peaks, corresponding to the two-step martensitic transformation (A→R→M). When the temperature reaches 510 °C, a single peak emerges, indicative of a one-step martensitic transformation (A→M). For all heat treatment temperatures, the DSC heating curves show a single peak, corresponding to the reverse martensitic transformation (M→A), where the R-phase has fully transformed into the M-phase. The phase transformation behavior of NiTi alloys differs during heating and cooling cycles. During heating, only a single peak corresponding to the reverse martensitic transformation (M→A) is observed. However, during cooling, two peaks appear, corresponding to the A→R→M phase transformation sequence. This difference arises due to the distinct mechanisms at play during heating and cooling. The formation of the R-phase during cooling is a consequence of the intermediate phase between martensite and austenite, which stabilizes under cooling conditions, while the reverse transition from martensite to austenite occurs as a single step during heating.

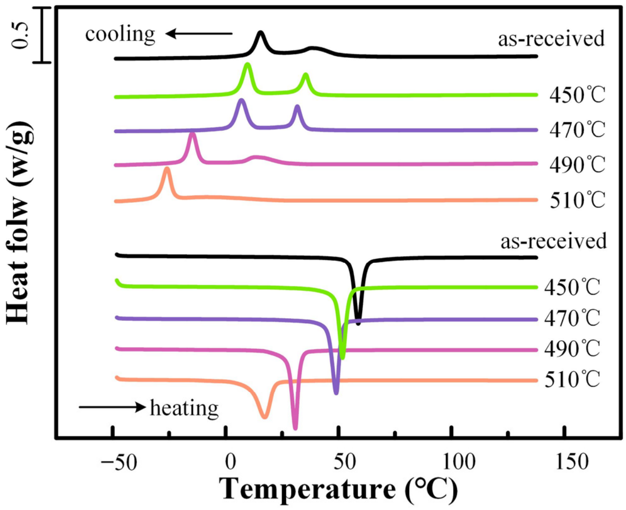

Figure 3. The DSC results of NiTi alloy after 10 min of heat treatment.

In summary, increasing the temperature or duration of heat treatment leads to a transition from a two-step martensitic transformation to a more stable one-step martensitic transformation in NiTi alloys. The phase transformation type and temperature of NiTi alloys can be modified and programmed through the heat treatment process.

3.2. Temperature Response of Vibration Isolation Structure

NiTi alloys exhibit excellent electrical conductivity, enabling the adjustment of the alloy's loading temperature through electrical heating. This impacts the alloy's superelasticity and shape memory properties, facilitating the programming and adjusting of the vibration isolation structure's performance.

As shown in Figure 4, the 'ON' label refers to the activation of the power supply, where voltage is applied to the NiTi alloy beams, and the 'OFF' label refers to the state where no voltage is applied, meaning the heating is turned off. The temperature increase is observed only when the power supply is turned 'ON' and current flows through the alloy beams. The temperature of the NiTi alloy horizontal and vertical cosine beams can be rapidly adjusted by varying the voltage of the power supply. At a voltage of 1 V, the temperature of the NiTi alloy cosine beam reaches 25 °C; at 2 V, it rises to 40.2 °C; and at 7 V, the temperature can increase to 79.8 °C. As the voltage increases, the temperature curve shows an approximately linear increase. Accordingly, a constant current of 6 A is selected, and tests on the alloy structure are conducted at 1 V, 2 V, and 7 V to study the effect of temperature on its static compression and dynamic vibration isolation performance.

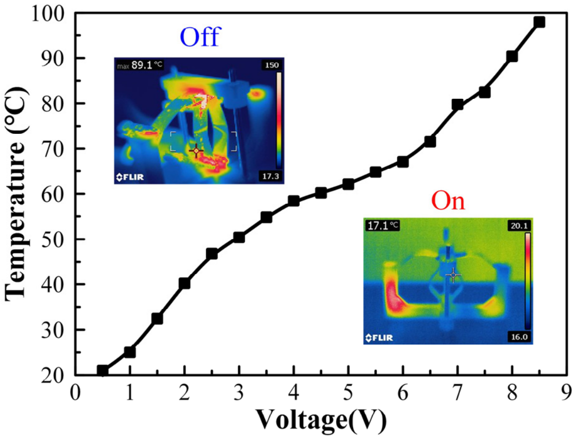

Figure 4. The heating temperature of the NiTi alloy vibration isolation structure at different voltages.

3.3. The Static Mechanical Performance of NiTi Alloy

The horizontal cosine beam provides negative stiffness, while the vertical cosine beam offers positive stiffness. By adjusting the design parameters of beams, the vibration isolation structure can exhibit various stiffness characteristics (positive, zero, and negative). The DSC test results demonstrate that the heat treatment process can alter the phase transformation temperature of the alloy. It is notable that NiTi alloys subjected to different heat treatment processes demonstrate varying mechanical properties (such as elastic modulus and yield strength) at the same testing temperature. Therefore, by programming the heat treatment processes of the horizontal and vertical cosine beams, the vibration isolation structure can be made to exhibit a range of stiffness characteristics at different testing temperatures. This makes it suitable for use in a variety of dynamic vibration isolation scenarios.

As a reference, the mechanical properties of the untreated samples are tested at different temperatures (25 °C, 60 °C, 80 °C), as shown in Figure 5.

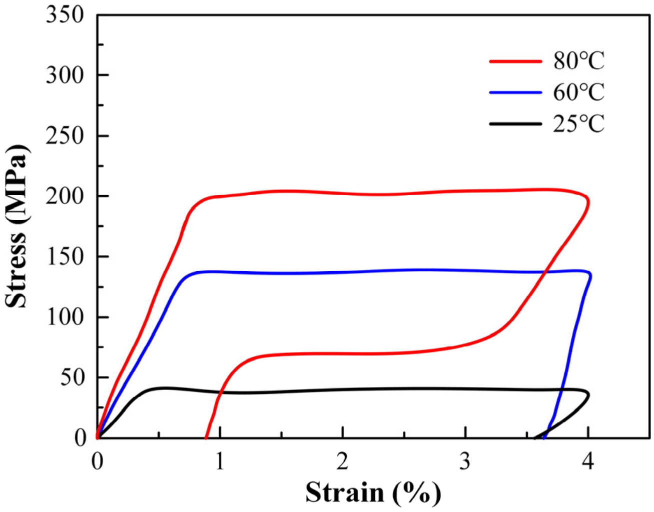

Figure 5. The mechanical properties of NiTi alloy at different temperatures without heat treatment.

When the testing temperature is below the M_f, the alloy exhibits shape memory characteristics. Conversely, when the temperature exceeds the A_f, the alloy displays superelasticity. It is noteworthy that within the temperature range between these two points, the alloy possesses both characteristics. According to Table 3, the phase transformation temperatures of the untreated NiTi alloy are as follows: M_f at 12.04 °C, M_s at 18.93 °C, A_s at 55.12 °C, and A_f at 64.34 °C. The results demonstrate that at both 25 °C and 60 °C, the alloy displays both shape memory characteristics and superelasticity. At 60 °C, the martensite phase within the alloy is observed to diminish, while the austenite phase is noted to increase, resulting in a gradual elevation in the plateau of the stress–strain curve. At 80 °C, the alloy undergoes a relatively complete reverse martensitic transformation, resulting in an increase in the austenite content and demonstrating superelasticity.

At 450 °C, holding times of 5, 10, 15, and 20 min are applied to examine the effect of heat treatment duration on the mechanical properties of NiTi alloy, as shown in Figure 6. Figure 6a illustrates that when the holding time is set at 5 min, the NiTi alloy's properties transition from shape memory behavior to the combination of memory and superelastic characteristics as the test temperature rises from 25 °C to 60 °C. At 80 °C, the alloy demonstrates full superelasticity, with the austenite phase dominating its internal structure.

As the test temperature rises from 25 °C to 60 °C and 80 °C, the holding time of 10 min reveals that the NiTi alloy changes from shape memory to superelastic behavior (Figure 6b). The test results are similar to those obtained with a holding time of 10 min when the holding times are 15 and 20 min, as shown in Figure 6c,d. As a result, extending the holding time during heat treatment increases the austenite phase content in the alloy, enabling the alloy to transition from shape memory behavior to superelastic behavior. The stress–strain curves at different heat treatment temperatures show similar maximum strains, even after treating the alloy at 510 °C. This can be attributed to the alloy's phase transformation characteristics, where the alloy transitions to a stable austenite phase at high temperatures, resulting in a more uniform strain response across all tested conditions.

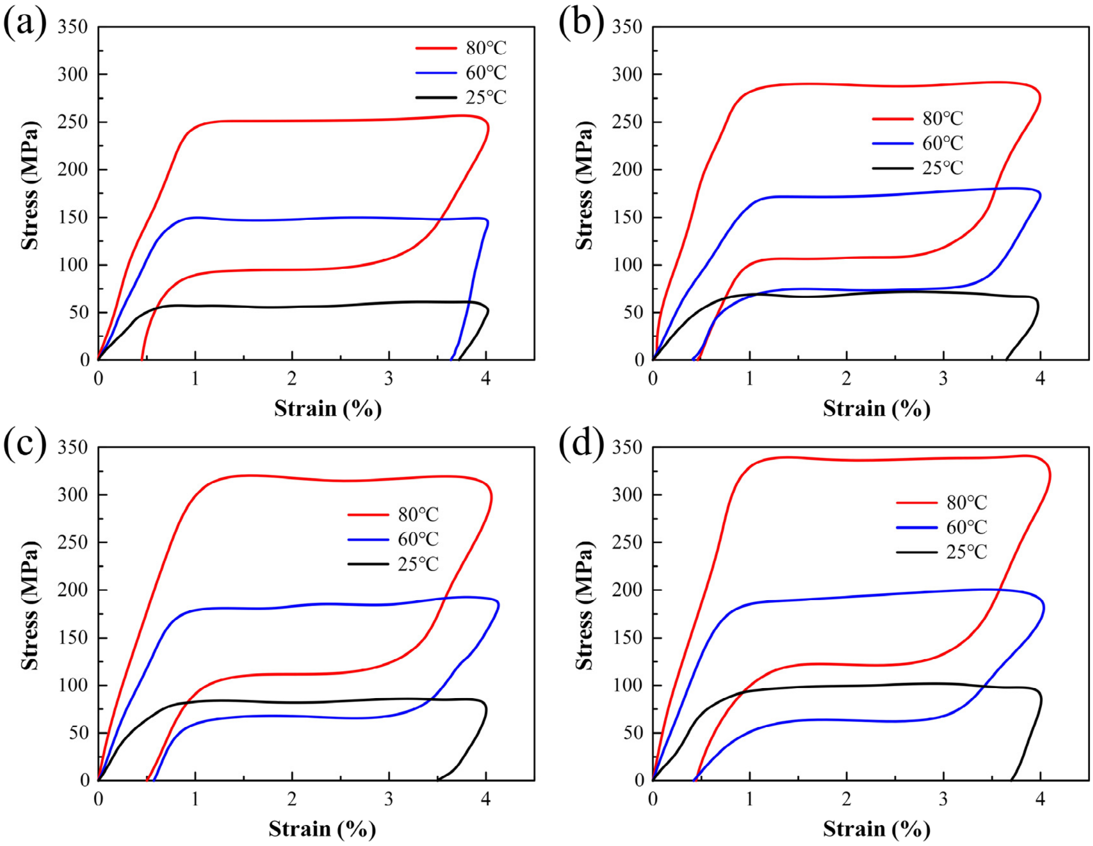

Figure 6. The effect of heat treatment time on the tensile properties of NiTi alloy: (**a**) 5 min. (**b**) 10 min. (**c**) 15 min. (**d**) 20 min.

With a heat treatment holding time of 10 min, the heat treatment temperatures are set at 450 °C, 470 °C, 490 °C, and 510 °C to investigate their effects on the mechanical properties of NiTi alloys, as shown in Figure 7. Figure 7a,b illustrate the effects of heat treatment temperatures of 450 °C and 470 °C on the NiTi alloy. As the testing temperature increases from 25 °C to 60 °C, the alloy transitions from shape memory behavior to a memory-superelastic composite behavior. At 80 °C, the alloy exhibits superelasticity, with its performance predominantly governed by the austenite phase. Therefore, the increase in the austenite phase with increasing heat treatment temperature leads to the transformation of the shape memory behavior into superelastic behavior in the alloy.

To conclude, the phase transformation temperature of NiTi alloy shows a gradual decrease with an increase in heat treatment temperature or holding time. An increase in the austenite phase content in the alloy results in elevated plateau stress on the stress–strain curve. Consequently, the alloy transitions from shape memory to superelastic properties.

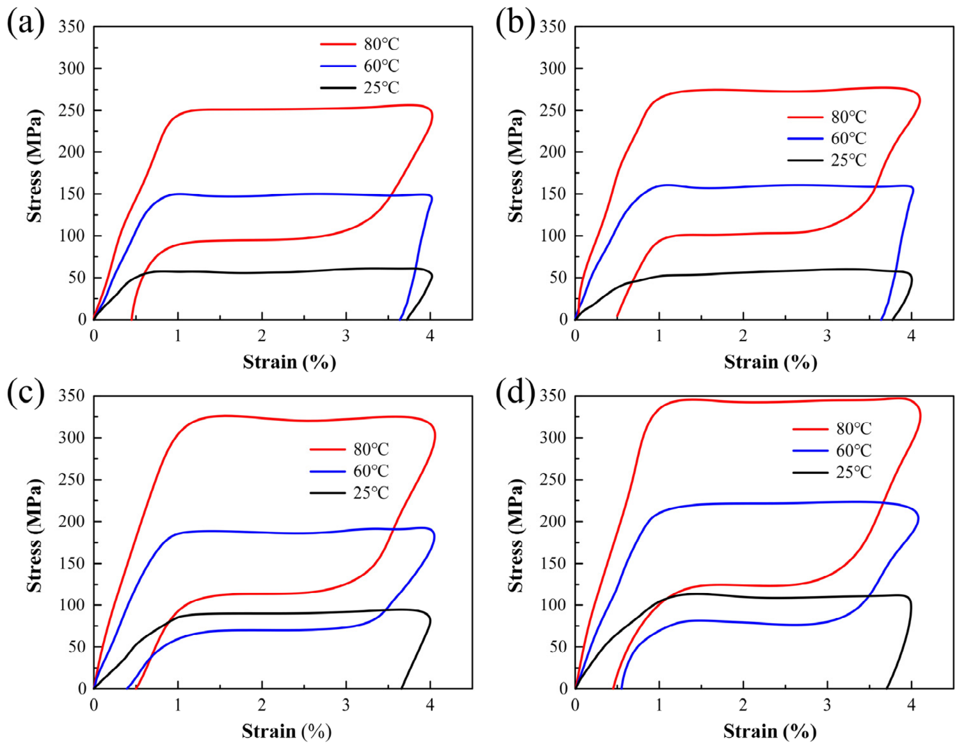

Figure 7. The effect of heat treatment temperature on the tensile properties of NiTi Alloy: (**a**) 450 °C. (**b**) 470 °C. (**c**) 490 °C. (**d**) 510 °C.

3.4. The Heat Treatment for the Static Response of Structure

Theoretical analysis shows that the horizontal cosine beam provides negative stiffness, while the vertical cosine beam provides positive stiffness. By adjusting the parameters of the horizontal and vertical cosine beams, the vibration isolation structure can exhibit different stiffness characteristics (positive, zero, and negative). DSC test results indicate that the heat treatment process can alter the phase transition temperature of the alloy. NiTi alloys subjected to different heat treatment processes can exhibit varying mechanical properties (such as elastic modulus and yield strength) at the same testing temperature. Therefore, by programming the heat treatment processes of the horizontal and vertical cosine beams, the vibration isolation structure can present various stiffness characteristics at different testing temperatures, making it applicable in dynamically changing vibration isolation scenarios.

The stiffness modes (positive, zero, and negative stiffness) shown in Figure 8b are determined using quasi-static compression tests conducted on vibration isolation structures composed of horizontal and vertical cosine beams at different test temperatures under various heat treatment conditions. The force–displacement curves obtained from these tests are analyzed to calculate the stiffness performance of the structures. The transitions between stiffness modes are identified based on changes in the slope of the force–displacement curves, representing positive, zero, and negative stiffness characteristics. As shown in Figure 8b, experiments conducted on the vibration isolation structure with varying heat treatment times (5 min, 10 min, 15 min, 20 min) and temperatures (450 °C, 470 °C, 490 °C, 510 °C) allow for the observation of three mechanical types at different testing temperatures (25 °C, 40 °C, 80 °C), including positive stiffness, zero stiffness, and negative stiffness. The heat treatment temperature of the horizontal cosine beam alloy is defined as T_{H}, the heat treatment temperature of the vertical cosine beam alloy as T_{V}, the heat treatment time of the horizontal cosine beam alloy as TI_{H}, and the heat treatment time of the vertical cosine beam alloy as TI_{V}, with zero representing the unprocessed cosine beam. The stiffness of the vibration isolation structure depends on the heat treatment of the horizontal and vertical cosine beams. As shown in Figure 8c,d, the experimental results indicate that increasing the heat treatment temperature and time of the horizontal cosine beam will result in the gradual transition of the vibration isolation structure from positive stiffness to zero stiffness, or from zero stiffness to negative stiffness at 25 °C. Conversely, increasing the heat treatment temperature and time of the vertical cosine beam will cause the transition from negative stiffness to zero stiffness to positive stiffness. The test results at 40 °C and 80 °C exhibit similar trends to those at 25 °C, as shown in Figure 8e–h.

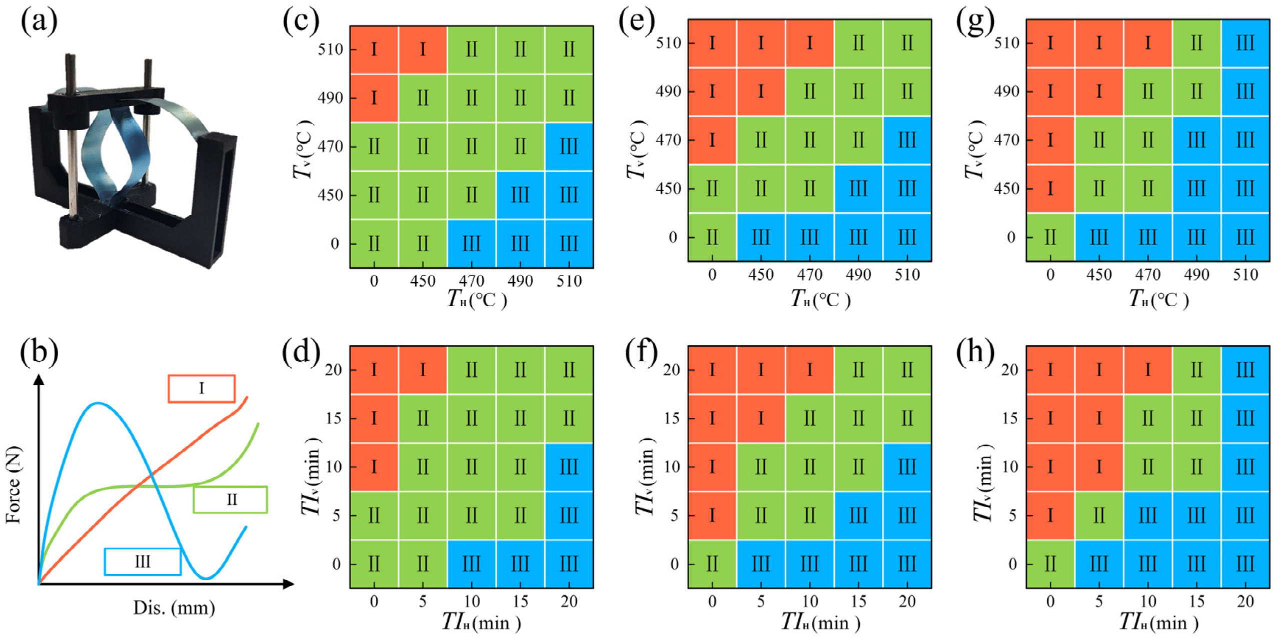

(c)

T_V(°C) \ T_H(°C)	0	450	470	490	510
510	I	I	II	II	II
490	I	II	II	II	II
470	II	II	II	II	III
450	II	II	II	III	III
0	II	II	III	III	III

(e)

T_V(°C) \ T_H(°C)	0	450	470	490	510
510	I	I	I	II	II
490	I	I	II	II	II
470	I	II	II	II	III
450	II	II	II	III	III
0	II	III	III	III	III

(g)

T_V(°C) \ T_H(°C)	0	450	470	490	510
510	I	I	I	II	III
490	I	I	II	II	III
470	I	II	II	III	III
450	I	II	II	III	III
0	II	III	III	III	III

(d)

TI_V(min) \ TI_H(min)	0	5	10	15	20
20	I	I	II	II	II
15	I	II	II	II	II
10	I	II	II	II	III
5	II	II	II	II	III
0	II	II	III	III	III

(f)

TI_V(min) \ TI_H(min)	0	5	10	15	20
20	I	I	I	II	II
15	I	I	II	II	II
10	I	II	II	II	III
5	I	II	II	III	III
0	II	III	III	III	III

(h)

TI_V(min) \ TI_H(min)	0	5	10	15	20
20	I	I	I	II	III
15	I	I	II	II	III
10	I	I	II	II	III
5	I	II	III	III	III
0	II	III	III	III	III

Figure 8. The influence of heat treatment conditions of horizontal and vertical cosine beams on structural stiffness performance: (**a**) The physical diagram of the vibration isolation structure. (**b**) The three stiffness modes of vibration isolation structure, I, positive stiffness, II, zero stiffness, III, negative stiffness. At 5 min heat treatment time, the effect of heat treatment temperature for horizontal and vertical cosine beams on the stiffness of vibration isolation structures with test temperatures of (**c**) 25 °C, (**e**) 40 °C, and (**g**) 80 °C. At 450 °C heat treatment temperature, the effect of heat treatment time for horizontal and vertical cosine beams on the stiffness of vibration isolation structures with test temperatures of (**d**) 25 °C, (**f**) 40 °C, and (**h**) 80 °C.

In consideration of the internal composition of the alloy, which is comprised of martensite and/or austenite, it can be observed that the content of internal austenite increases gradually as a result of increasing the heat treatment temperature/time. This phenomenon leads to a corresponding increase in the modulus of the alloy. In the vibration isolation structure, the horizontal cosine beam provides negative stiffness, which becomes more significant as the heat treatment temperature/time increases, resulting in a gradual transition from positive to zero stiffness or from zero to negative stiffness. Similarly, the vertical cosine beam provides positive stiffness, leading to a gradual transition from negative to zero to positive stiffness. We conduct quasi-static mechanical tests on the vibration isolation structures to obtain force–displacement curves, which use to evaluate the stiffness performance of the structures under different heat treatment conditions. These results inform the experimental design of subsequent vibration isolation tests, allowing for a targeted investigation of the isolation performance.

3.5. The Static Response of the NiTi Alloy Vibration Isolation Structure

Given the excellent performance of zero-stiffness structures in cushioning and vibration isolation applications, we selected four groups of vibration isolation structures with zero-stiffness characteristics for subsequent vibration isolation testing. The heat treatment conditions of these structures are detailed in Table 5.

Table 5. The heat treatment condition for cosine beam of the vibration isolation structure.

Name	Horizontal Cosine Beam	Vertical Cosine Beam
S1	None	None
S2	450 °C, 5 min	450 °C, 5 min
S3	470 °C, 5 min	450 °C, 5 min
S4	470 °C, 5 min	490 °C, 5 min

As illustrated in Figure 9, the stiffness characteristics of the vibration isolation structures exhibit notable differences under varying test temperatures. The results of the static compression test demonstrate that when the temperature is 25 °C, 40 °C, and 80 °C, the quasi-zero stiffness reaction/peak forces of S1 are approximately 5.5 N, 7.5 N, and 10 N, respectively (Figure 9a). In the quasi-zero stiffness range of S2, the reaction force/peak force is approximately 7 N, 8.5 N, and 12 N at 25 °C, 40 °C, and 80 °C, as illustrated in Figure 9b. Figure 9c illustrates that the quasi-zero stiffness reaction force/peak force of S3 is approximately 8 N, 10 N, and 13.5 N at 25 °C, 40 °C, and 80 °C, respectively. Figure 9d depicts that the quasi-zero stiffness reaction force/peak force of S4 is approximately 10 N, 12.5 N, and 16.5 N at 25 °C, 40 °C, and 80 °C.

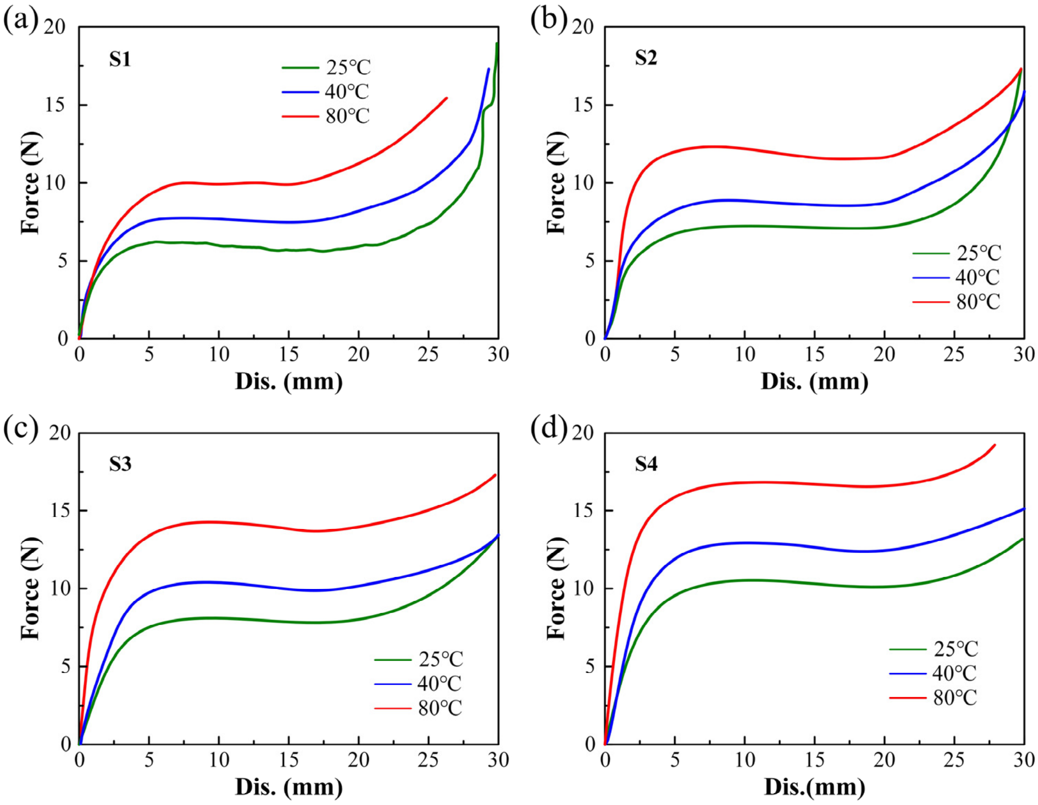

Figure 9. The quasi-static compression experimental results of the vibration isolation structure at different test temperatures (25 °C, 40 °C, 80 °C): (**a**) S1. (**b**) S2. (**c**) S3. (**d**) S4.

The zero-stiffness reaction forces/peak forces of the four structures exhibited a gradual increase as the test temperature increased from 25 °C to 60 °C and then to 80 °C. At 25 °C, the NiTi alloy is composed of martensite and austenite phases. The martensite phase is characterized by a softer and more plastic nature, whereas the austenite phase exhibits a harder and more rigid quality. As the test temperature increases to 40 °C, the quantity of the austenite phase within the alloy rises. Upon reaching 80 °C, the alloy is composed entirely of the austenite phase. Consequently, the peak force of the four structures increases along with the test temperature. Furthermore, the quasi-zero stiffness displacement range of the four vibration isolation structures became narrower as the test temperature increased. For instance, S1 displays a broad quasi-zero stiffness displacement range (5 mm to 22.5 mm) at 25 °C, a narrower range (5 mm to 17.5 mm) at 40 °C, and the narrowest range (5 mm to 15 mm) at 80 °C.

The design of the vibration isolation structure can control the performance of the long-strain platform and the peak force of zero stiffness by programming the temperature and time of the thermal treatment of the vertical and horizontal cosine beams, achieving adjustability of the stiffness of the vibration isolation structure.

3.6. Vibration Isolation Performances of the NiTi Alloy Structures

The vibration isolation performance of S1, S2, S3, and S4 was evaluated through experimental analysis using a custom-built isolation system. The vertical and horizontal cosine beams are subjected to an electric current, and the temperature of the four structures is subsequently measured using an infrared thermal imaging camera. The excitation voltage amplitude is set to 0.5 V, and a balanced weight is applied to each of the four isolation structures. The applied weights corresponding to S1 are 0.55 kg, 0.75 kg, and 1.0 kg at 25 °C, 40 °C, and 80 °C, respectively. The applied weights corresponding to S2 are 0.7 kg, 0.85 kg, and 1.2 kg at 25 °C, 40 °C, and 80 °C, respectively. The applied weights corresponding to S3 are 0.8 kg, 1.0 kg, and 1.35 kg at 25 °C, 40 °C, and 80 °C, respectively. The applied weights corresponding to S4 are 1.0 kg, 1.25 kg, and 1.65 kg at 25 °C, 40 °C, and 80 °C, respectively. Furthermore, a rapid frequency sweep from 1 Hz to 100 Hz is conducted on all four structures.

As illustrated in Figure 10, the structural vibration isolation frequency range exhibits gradually narrowed as the test temperature increases. Figure 10a illustrates the experimental results pertaining to the vibration isolation performance of S1 at varying test temperatures. At 25 °C, the vibration isolation frequency range of S1 is 8.7 Hz to 100 Hz. At 40 °C, this range narrows to 11.12 Hz to 100 Hz. At 80 °C, the range narrows further, to 13.38 Hz to 100 Hz. This phenomenon can be attributed to the observation that S1 exhibits the longest strain plateau at a zero-stiffness curve at a test temperature of 25 °C, followed by 40 °C, and the shortest strain plateau at 80 °C. Therefore, S1 demonstrates the optimal vibration isolation performance at 25 °C. Similarly, S2 (Figure 10b), S3 (Figure 10c), and S4 (Figure 10d) demonstrate comparable performance trends. The vibration isolation performance varies significantly with temperature. For example, in the case of the S1 structure, the isolation frequency decreases from 13.38 Hz at 80 °C to 8.7 Hz at 25 °C, which can be attributed to the marked difference in the zero-stiffness displacement range at different temperatures. However, at the same temperature, the differences in isolation performance between the four structures are less pronounced, as shown in Figure 9, where the zero-stiffness displacement ranges at each temperature are similar, leading to comparable isolation frequencies.

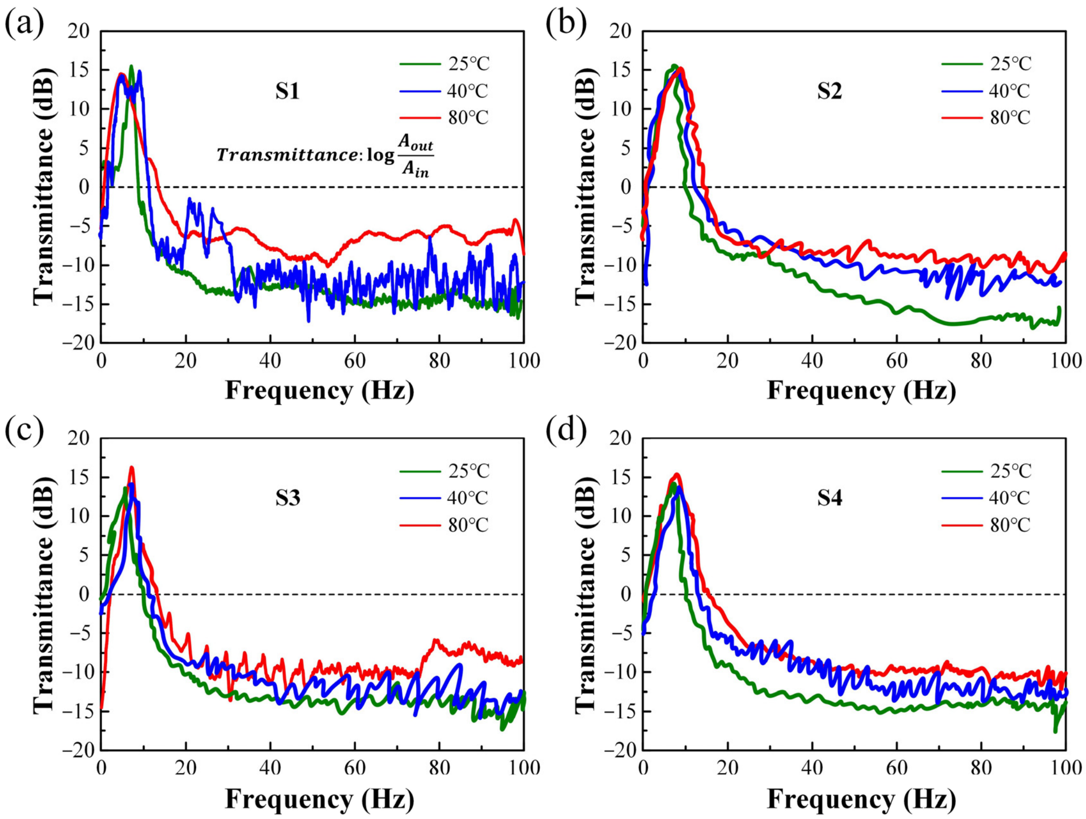

Figure 10. The transmissibility curve of the vibration isolation structure at different temperatures (25 °C, 40 °C, 80 °C): (**a**) S1. (**b**) S2. (**c**) S3. (**d**) S4.

4. Conclusions

This study designs and manufactures vibration isolation structures with adjustable material stiffness using NiTi shape memory alloys. The effects of heat treatment processes on the vibration isolation performance of structures are investigated. The influence of temperature control on the stiffness variation behavior and vibration isolation performance of the structure is analyzed, demonstrating that temperature control can adjust the vibration isolation performance. The vibration isolation structure consists of vertical and horizontal NiTi alloy beams. The impact of heat treatment processes (time and temperature) on the phase transition temperatures of NiTi alloy is studied, with results showing that the phase transition temperature of the alloy decreases as heat treatment temperature and time increase. Moreover, geometric and theoretical mechanical models of the vibration isolation structure composed of horizontal and vertical alloy beams are developed. The temperature response of the vibration isolation structure is studied, and the effects of four different heat treatment processes on the quasi-static mechanical properties of the isolation structure are explored. Experimental results show that the stiffness of the vibration isolation structure can be effectively adjusted by varying the applied temperature. Based on the above, vibration isolation performance tests are conducted on four groups of vibration isolation structures, confirming the adjustability of vibration isolation performance under temperature control.

Author Contributions: Conceptualization, Q.W., X.L., and S.W. (Shengsheng Wang); methodology, Q.W., B.L., and Z.W.; formal analysis, X.L., J.Q., and S.W. (Shengsheng Wang); investigation, Q.W., S.W. (Shengsheng Wang), and Z.W.; validation, X.L., S.W. (Siyang Wang), and J.J.; writing—original draft preparation, Q.W. and Z.W.; writing—review and editing, B.L., S.W. (Siyang Wang), and

Z.W.; supervision, J.Q., X.L., and J.J. All authors have read and agreed to the published version of the manuscript.

Funding: This work was supported by the research on driving mechanism and attitude control strategy of reconfigurable flexible chassis in hilly terrain under Grant SKLIAPE2023015 and the National Natural Science Foundation of China (No. 52305305).

Data Availability Statement: Measurement data are available from the authors upon request.

Conflicts of Interest: The authors declare no conflicts of interest.

References

1. Al Rifaie, M.; Abdulhadi, H.; Mian, A. Advances in mechanical metamaterials for vibration isolation: A review. *Adv. Mech. Eng.* **2022**, *14*, 16878132221082872. [CrossRef]
2. Zhou, W.Y.; Li, D.X.; Luo, Q.; Liu, K. Analysis and Testing of Microvibrations Produced by Momentum Wheel Assemblies. *Chin. J. Aeronaut.* **2012**, *25*, 640–649. [CrossRef]
3. Deng, X.; Pan, Z.W.; Xing, J.W.; Zhang, Z.Y.; Li, Y.X.; Yan, M.S.; Dong, X.M. Controllability analysis and intelligent control of magnetorheological whole-satellite under small amplitude and medium-high frequency vibration. *J. Intell. Mater. Syst. Struct.* **2023**, *34*, 229–248. [CrossRef]
4. Li, L.; Wang, L.; Yuan, L.; Zheng, R.; Wu, Y.P.; Sui, J.; Zhong, J. Micro-vibration suppression methods and key technologies for high-precision space optical instruments. *Acta Astronaut.* **2021**, *180*, 417–428. [CrossRef]
5. Rivin, E.I. Vibration isolation of precision equipment. *Precis. Eng.* **1995**, *17*, 41–56. [CrossRef]
6. Yan, G.; Zou, H.-X.; Wang, S.; Zhao, L.-C.; Wu, Z.-Y.; Zhang, W.-M. Bio-inspired vibration isolation: Methodology and design. *Appl. Mech. Rev.* **2021**, *73*, 020801. [CrossRef]
7. Ma, R.; Bi, K.; Hao, H. Inerter-based structural vibration control: A state-of-the-art review. *Eng. Struct.* **2021**, *243*, 112655. [CrossRef]
8. Zeng, X.; Xu, J.; Han, B.; Zhu, Z.; Wang, S.; Wang, J.; Yang, X.; Cai, R.; Du, C.; Zeng, J. A Review of Linear Compressor Vibration Isolation Methods. *Processes* **2024**, *12*, 2210. [CrossRef]
9. Niu, M.-Q.; Chen, L.-Q. Analysis of a bio-inspired vibration isolator with a compliant limb-like structure. *Mech. Syst. Signal Process.* **2022**, *179*, 109348. [CrossRef]
10. Ji, J.; Zhang, N. Suppression of the primary resonance vibrations of a forced nonlinear system using a dynamic vibration absorber. *J. Sound Vib.* **2010**, *329*, 2044–2056. [CrossRef]
11. Ning, C.; Zhichun, Y.; Te, Y.; Yizhou, S.; Wei, T.; Yanlong, X. Design of low-frequency circular metastructure isolators with high-load-bearing capacity. *Chin. J. Aeronaut.* **2024**, *37*, 207–220.
12. Yan, G.; Lu, J.-J.; Qi, W.-H.; Liu, F.-R.; Yan, H.; Zhao, L.-C.; Wu, Z.-Y.; Zhang, W.-M. Linear and nonlinear stiffness compensation for low-frequency vibration isolation: A comparative study. *Nonlinear Dyn.* **2024**, *112*, 5955–5973. [CrossRef]
13. Chen, N.; Yang, Z.; Zuo, A.; Jiang, P.; Jin, S.; Xu, Y. Bandgap regulations of longitudinal wave for a nonlinear metastructure isolator with high-static-low-dynamic stiffness. *Compos. Struct.* **2024**, *327*, 117706. [CrossRef]
14. Yan, B.; Yu, N.; Wu, C.Y. A state-of-the-art review on low-frequency nonlinear vibration isolation with electromagnetic mechanisms. *Appl. Math. Mech.* **2022**, *43*, 1045–1062. [CrossRef]
15. Abbasi, A.; Khadem, S.E.; Bab, S. Vibration control of a continuous rotating shaft employing high-static low-dynamic stiffness isolators. *J. Vib. Control* **2016**, *24*, 760–783. [CrossRef]
16. Huang, X.C.; Liu, X.T.; Sun, J.Y.; Zhang, Z.Y.; Hua, H.X. Effect of the system imperfections on the dynamic response of a high-static-low-dynamic stiffness vibration isolator. *Nonlinear Dyn.* **2014**, *76*, 1157–1167. [CrossRef]
17. Zuo, S.; Wang, D.Y.; Zhang, Y.S.; Luo, Q.T. Design and testing of a parabolic cam-roller quasi-zero-stiffness vibration isolator. *Int. J. Mech. Sci.* **2022**, *220*, 107146. [CrossRef]
18. Jiang, G.Q.; Jing, X.J.; Guo, Y.Q. A novel bio-inspired multi-joint anti-vibration structure and its nonlinear HSLDS properties. *Mech. Syst. Sig. Process.* **2020**, *138*, 106552. [CrossRef]
19. Zhao, F.; Cao, S.Q.; Luo, Q.T.; Li, L.Q.; Ji, J.C. Practical design of the QZS isolator with one pair of oblique bars by considering pre-compression and low-dynamic stiffness. *Nonlinear Dyn.* **2022**, *108*, 3313–3330. [CrossRef]
20. Dong, G.X.; Zhang, X.N.; Xie, S.L.; Yan, B.; Luo, Y.J. Simulated and experimental studies on a high-static-low-dynamic stiffness isolator using magnetic negative stiffness spring. *Mech. Syst. Sig. Process.* **2017**, *86*, 188–203. [CrossRef]
21. Yu, C.Y.; Fu, Q.D.; Zhang, J.R.; Zhang, N. The vibration isolation characteristics of torsion bar spring with negative stiffness structure. *Mech. Syst. Sig. Process.* **2022**, *180*, 109378. [CrossRef]
22. Ma, Z.; Zhou, R.; Yang, Q. Recent advances in quasi-zero stiffness vibration isolation systems: An overview and future possibilities. *Machines* **2022**, *10*, 813. [CrossRef]

23. Yan, G.; Zou, H.-X.; Wang, S.; Zhao, L.-C.; Gao, Q.-H.; Tan, T.; Zhang, W.-M. Large stroke quasi-zero stiffness vibration isolator using three-link mechanism. *J. Sound Vib.* **2020**, *478*, 115344. [CrossRef]
24. Ye, K.; Ji, J.; Brown, T. Design of a quasi-zero stiffness isolation system for supporting different loads. *J. Sound Vib.* **2020**, *471*, 115198. [CrossRef]
25. Etawy, M.S.; Nassar, G.E.; Mohammed, N.; Nawar, S.H.; Hassabo, A.G. 4D Printing of Stimuli-Responsive Materials. *J.Text. Color. Polym. Sci.* **2024**, *21*, 241–258. [CrossRef]
26. Abavisani, I.; Rezaifar, O.; Kheyroddin, A. Multifunctional properties of shape memory materials in civil engineering applications: A state-of-the-art review. *J. Build. Eng.* **2021**, *44*, 102657. [CrossRef]
27. Bogue, R. Shape-memory materials: A review of technology and applications. *Assem. Autom.* **2009**, *29*, 214–219. [CrossRef]
28. Sreekumar, M.; Nagarajan, T.; Singaperumal, M.; Zoppi, M.; Molfino, R. Critical review of current trends in shape memory alloy actuators for intelligent robots. *Ind. Robot. Int. J.* **2007**, *34*, 285–294. [CrossRef]
29. Behera, A.; Behera, A. Shape-memory materials. In *Advanced Materials: An Introduction to Modern Materials Science*; Springer Nature: Berlin/Heidelberg, Germany, 2022; pp. 1–42.
30. Ebrahimi, M.; Attarilar, S.; Gode, C.; Kandavalli, S.R.; Shamsborhan, M.; Wang, Q. Conceptual analysis on severe plastic deformation processes of shape memory alloys: Mechanical properties and microstructure characterization. *Metals* **2023**, *13*, 447. [CrossRef]
31. Park, S.K.; Diao, Y. Martensitic transition in molecular crystals for dynamic functional materials. *Chem. Soc. Rev.* **2020**, *49*, 8287–8314. [CrossRef]
32. Kim, M.S.; Heo, J.K.; Rodrigue, H.; Lee, H.T.; Pané, S.; Han, M.W.; Ahn, S.H. Shape Memory Alloy (SMA) Actuators: The Role of Material, Form, and Scaling Effects. *Adv. Mater.* **2023**, *35*, 2208517. [CrossRef] [PubMed]
33. Lee, S.E.; Jung, H.J.; Lee, K.H. Motivating Collaborative Consumption in Fashion: Consumer Benefits, Perceived Risks, Service Trust, and Usage Intention of Online Fashion Rental Services. *Sustainability* **2021**, *13*, 1804. [CrossRef]
34. Qiu, J.; Lang, J.H.; Slocum, A.H. A curved-beam bistable mechanism. *J. Microelectromech. Syst.* **2004**, *13*, 137–146. [CrossRef]
35. Cai, C.Q.; Zhou, J.X.; Wu, L.C.; Wang, K.; Xu, D.L.; Ouyang, H.J. Design and numerical validation of quasi-zero-stiffness metamaterials for very low-frequency band gaps. *Compos. Struct.* **2020**, *236*, 111862. [CrossRef]
36. Fan, H.G.; Yang, L.J.; Tian, Y.C.; Wang, Z.W. Design of metastructures with quasi-zero dynamic stiffness for vibration isolation. *Compos. Struct.* **2020**, *243*, 112244. [CrossRef]
37. Lu, H.J.; Meng, L.X.; Wang, J.K.; Wang, Y.; Zhang, L.Z. Design and Performance Study of Metamaterial with Quasi-zero Stiffness Characteristics Based on Human Body Structure. *J. Vib. Eng. Technol.* **2024**, *12*, 633–648. [CrossRef]
38. Feng, Y.; Liu, B.; Wan, X.; Liu, Q.; Lin, X.; Wang, P. Influence of processing parameter on phase transformation and superelastic recovery strain of laser solid forming NiTi alloy. *J. Alloys Compd.* **2022**, *908*, 164568. [CrossRef]
39. Pu, Z.; Du, D.; Wang, K.; Liu, G.; Zhang, D.; Wang, X.; Chang, B. Microstructure, phase transformation behavior and tensile superelasticity of NiTi shape memory alloys fabricated by the wire-based vacuum additive manufacturing. *Mater. Sci. Eng. A* **2021**, *812*, 141077. [CrossRef]
40. Ma, J.; Yu, L.; Yang, Q.; Liu, J.; Yang, L. High-Superelasticity NiTi Shape Memory Alloy by Directed Energy Deposition-Arc and Solution Heat Treatment. *Acta Metall. Sinica* **2024**, *37*, 132–144. [CrossRef]
41. Du, F.; Deng, L.; Zhang, M.; Gong, P.; Jin, J.; Liu, F.; Wang, X. Mechanical response and phase transformation characteristics of R-phase NiTi shape memory alloy under high strain rate compression. *Mater. Today Commun.* **2024**, *39*, 109353. [CrossRef]
42. Li, B.; Wang, B.; Wang, L.; Oliveira, J.; Cui, R.; Wang, Y.; Zhu, G.; Yu, J.; Su, Y. Effect of post-heat treatments on the microstructure, martensitic transformation and functional performance of EBF3-fabricated NiTi shape memory alloy. *Mater. Sci. Eng. A* **2023**, *871*, 144897. [CrossRef]
43. Hecker, S.; Harbur, D.; Zocco, T. Phase stability and phase transformations in Pu–Ga alloys. *Prog. Mater Sci.* **2004**, *49*, 429–485. [CrossRef]
44. Roitburd, A.; Kurdjumov, G. The nature of martensitic transformations. *Mater. Sci. Eng.* **1979**, *39*, 141–167. [CrossRef]